NANO LETTERS

pubs.acs.org/NanoLett Letter

In Liquid Infrared Scattering Scanning Near-Field Optical Microscopy for Chemical and Biological Nanoimaging

Brian T. O'Callahan, Kyoung-Duck Park, Irina V. Novikova, Tengyue Jian, Chun-Long Chen, Eric A. Muller, Patrick Z. El-Khoury, Markus B. Raschke,* and A. Scott Lea*

Cite This: *Nano Lett.* 2020, 20, 4497−4504 Read Online

ACCESS | Metrics & More | Article Recommendations | Supporting Information

ABSTRACT: Imaging biological systems with simultaneous intrinsic chemical specificity and nanometer spatial resolution in their typical native liquid environment has remained a long-standing challenge. Here, we demonstrate a general approach of chemical nanoimaging in liquid based on infrared scattering scanning near-field optical microscopy (IR *s*-SNOM). It is enabled by combining AFM operation in a fluid cell with evanescent IR illumination via total internal reflection, which provides spatially confined excitation for minimized IR water absorption, reduced far-field background, and enhanced directional signal emission and sensitivity. We demonstrate in-liquid IR *s*-SNOM vibrational nanoimaging and conformational identification of catalase nanocrystals and spatio-spectral analysis of biomimetic peptoid sheets with monolayer sensitivity and chemical specificity at the few zeptomole level. This work establishes the principles of in-liquid and *in situ* IR *s*-SNOM spectroscopic chemical nanoimaging and its general applicability to biomolecular, cellular, catalytic, electrochemical, or other interfaces and nanosystems in liquids or solutions.

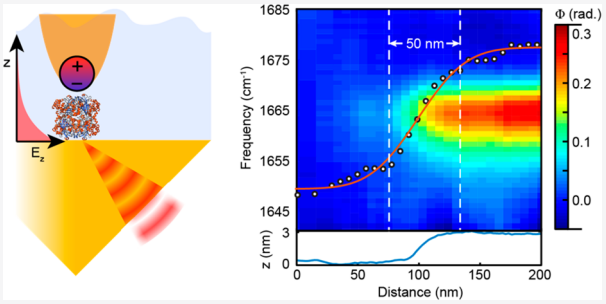

KEYWORDS: *Nanospectroscopy, bioimaging, in-liquid, in situ*

INTRODUCTION

Fundamental biological processes such as ion transfer across cell membranes and protein folding rely on complex nanoscale molecular organization and dynamical interactions in aqueous environments. Gaining insight into these processes requires imaging techniques that afford simultaneous nanoscale spatial resolution, chemical specificity, and in-liquid operation. While electron microscopy (EM) allows nanometer spatial resolution of biomolecular structures in liquid,[1−5] its general applicability has remained challenging due to electron beam induced perturbation and degradation of the molecular matter.[6,7] Cryo-EM significantly increases the damage threshold and enables even atomic resolution 3D reconstructions of the analyte in a vitrified solid,[8] but direct imaging of the dynamics of molecules *in situ* remains a significant challenge.

Directly probing the dynamics of biomolecules in their in-liquid/*in vivo* environment is achieved using different optical *in situ* super-resolution techniques, such as stochastic optical reconstruction microscopy (STORM) or photoactivated localization microscopy (PALM), which provide nanometer spatial resolution and even video rate imaging.[9−13] However, these super-resolution methods rely on molecular labeling of the target structure with a compatible fluorophore.

Different vibrational nanospectroscopy and imaging techniques that provide intrinsic chemical specificity and contrast with nanometer spatial resolution have recently emerged.[14−16] Specifically, tip-enhanced Raman spectroscopy (TERS) in liquids is facilitated by the general transparency of water to the visible excitation and Raman emission.[14,17,18] Yet, TERS applications to biological systems are hindered by their typically low spontaneous Raman scattering cross sections.[19] At infrared frequencies, driven by the strong and structurally specific vibrational modes of proteins and their conformers,[20,21] in-liquid IR nanoimaging has been demonstrated in photothermal induced resonance (PTIR) which measures IR absorption by monitoring sample thermal expansion.[22−25] However, for decreasing sample thicknesses the background from thermal expansion of the liquid itself can reduce image contrast and sensitivity.[23]

Alternatively, infrared scattering-type scanning near-field optical microscopy (IR *s*-SNOM) provides an all-optical technique for minimally invasive chemically specific nanoimaging which is particularly well suited for the study of biological matter.[15,26] To circumvent the unavoidable and significant broadband IR absorption of water and aqueous

Received: March 24, 2020
Revised: April 18, 2020
Published: May 1, 2020

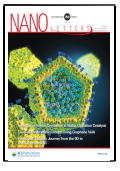

https://dx.doi.org/10.1021/acs.nanolett.0c01291
Nano Lett. 2020, 20, 4497−4504

solutions, various approaches have been pursued with the atomic force microscopy (AFM) operating in air and the liquid phase separated by a thin IR-transparent membrane.[27−29] Analytes are then interrogated by the tens of nanometers spatial extent of the tip near-field which enables IR nanospectroscopy of molecules near the membrane interface. However, no broadly applicable fully in-liquid IR s-SNOM approach has yet been established.

Here, we demonstrate in-liquid and *in situ* IR *s*-SNOM with in-liquid AFM operation and total internal reflection (TIR) excitation as a universal approach to infrared nanospectroscopy of biological systems in their native environment. With optimized TIR conditions, our method affords vibrational signal enhancement, efficient collection of tip−sample dipole emission, and minimized IR absorption and undesirable far-field background. As examples, we show nanoimaging and conformational identification of catalase nanocrystals and spatio-spectral analysis of biomimetic peptoid sheets with extension to few zeptomole sensitivity and chemical specificity based on additional plasmonic field enhancement using metal nanoplatelets. Our results are supported by electromagnetic simulations and analytical modeling which demonstrate the potential of IR *s*-SNOM for general in-liquid and in situ nanoanalytical imaging.

Figure 1a shows the experimental schematic (see Methods for more details). An off-axis parabolic mirror (effective focal length f = 20.3 mm, NA ≈ 0.5) focuses mid-infrared (MIR) light into a ZnSe prism (n = 2.43) of an atomic force microscope designed to operate in liquid (AFM, AFM+ from Anasys Instruments). In this total internal reflection geometry, an evanescent field extends above the prism surface with 1/e decay length $\gamma \sim 500$ at excitation wavelength $\lambda = 6$ μm, and illuminates the tip−sample region. As in conventional *s*-SNOM implementations,[15,30,31] we detect the tip-backscattered optical field yet here coupled through the prism. The detector signal is amplified and sent to a lock-in amplifier (HF2LI, Zurich) which demodulates the optical signal at harmonics of the tip-tapping frequency Ω to filter out background from far-field scattering. Finite-difference time-domain (FDTD) simulations show a factor of >100 optical intensity enhancement is present in this geometry (Figure 2a). Samples are dropcast onto the prism and the AFM cantilever and sample region are immersed in DI water. The AFM is operated in tapping mode where the tip vertical position is adjusted to maintain constant tapping amplitude, and the prism is raster-scanned during image acquisition and translated laterally for coarse sample positioning.

Figure 1c shows the dependence of the tip-scattered signal on the tip−sample separation at the first and second harmonic of the tapping frequency. Both show near-surface confinement, with the second harmonic more spatially confined than the first harmonic, as expected.[31] The nanometric spatial confinement of the first harmonic signal observed indicates that it already provides adequate background subtraction and spatial resolution. This is not typically the case for conventional SNOM studies in which higher harmonics of the tip tapping frequency are typically needed to isolate the near-field signal from the large far-field background that arises from reflection and scattering off the tip-shaft and the sample surface. In the total internal reflection geometry, the laser excitation is confined to ∼500 nm from the prism surface, which is a much smaller region than the few tens of micrometers focused beam spot of a conventional *s*-SNOM. This smaller sampling

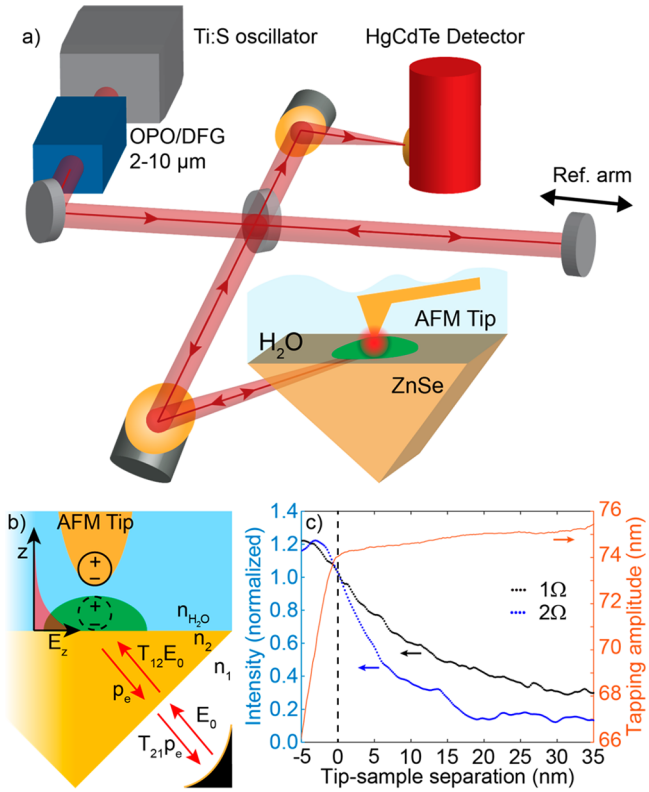

Figure 1. (a) Experimental schematic. MIR light is generated through an optical parametric oscillator and difference frequency generation (OPO/DFG) system pumped with a Ti:sapphire (Ti:S) oscillator. An OAPM directs the light into a ZnSe prism of an in-liquid AFM. Backscattered light is collected with the OAPM and detected with a HgCdTe detector. An asymmetric Michelson geometry is used to obtain spectra by sweeping the reference arm (ref. arm) position to obtain interferograms. (b) Detail of tip-illumination geometry. Optical field of strength E_o is focused into the prism (dielectric function n_2) with a parabolic mirror. The total internal reflection geometry creates an exponentially decaying evanescent field at the prism surface which excites tip−sample coupled dipole that radiates into the prism. (c) Approach curves showing the distance dependence of the near-field signal collected at the first and second harmonic of the tapping frequency (blue and black) with the AFM tapping amplitude shown in red.

volume results in a much weaker background source. Additionally, our geometry relies on coupling of the tip−sample dipole field into the ZnSe prism, which results in a significantly reduced probe volume compared to conventional SNOM. While higher harmonic demodulation slightly improves spatial resolution in conventional *s*-SNOM, it is typically at the expense of a factor of 5−10 worse signal-to-noise ratio.

As samples, we study two-dimensional nanosheets of a lipid-like peptoid composed of crystalline arrangement of linear chains of repeated amide groups and microcrystallites of catalase protein.[32,33] The peptoid nanosheets were synthesized using a previously reported evaporation-induced crystallization method[32] to create ∼4 nm thick sheets which provide a robust amide I response to assess our spatial resolution and sensitivity limit. The catalase crystallites were prepared according to a previously published protocol with few tens of nanometers thicknesses and hundreds of nanometers in size in lateral dimension.[33] As a canonical target of electron microscopy and diffraction studies, the known structure of catalase crystals can

https://dx.doi.org/10.1021/acs.nanolett.0c01291
Nano Lett. 2020, 20, 4497−4504

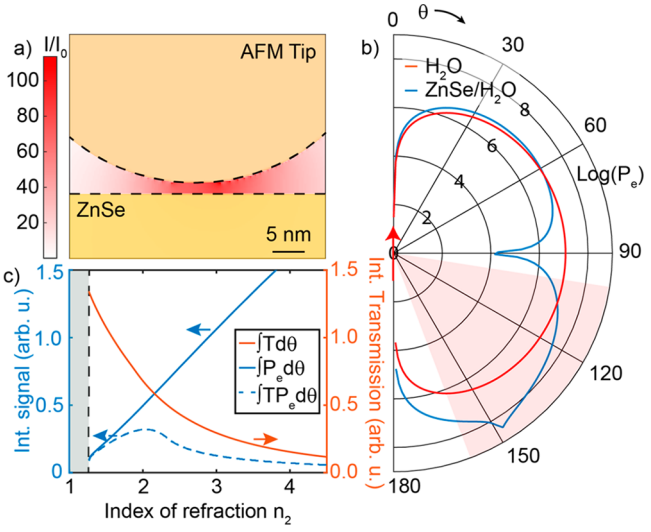

Figure 2. (a) Finite difference time domain simulations of the field structure of a Au tip (tip radius r = 30 nm) 2 nm above a ZnSe surface illuminated by IR light at 1785 cm^{-1} incident at 45° from normal. An intensity enhancement of >100 is present. (b) Polar plot of the emitted power of a dipole at the interface of a ZnSe/H_2O interface (n_1 = 1.265, n_2 = 2.43) (blue) and the order of magnitude weaker emission of a dipole immersed in water ($n_1 = n_2$ = 1.265, red line). The red shaded region indicates the collection angle of our setup. (c) Transmission coefficient T, dipole emission P_e, and detectable power TP_e are shown integrated over the solid angle of the parabolic mirror from a dipole on a surface as a function of the material dielectric function.

be used as a reference of the ability of TIR *s*-SNOM to perform conformational analysis of a natural protein in a liquid environment.[34]

RESULTS

Modeling of the In-Liquid IR Excitation. Our excitation/collection pathway relies on evanescent coupling between tip-excited polarization in the sample and propagating photons within the supporting prism. As shown in Figure 1b, an external illumination field E_0 transmits into the dielectric prism (index of refraction n_2) with transmission coefficient T_{12} and excites the tip−sample region. We model the resulting coupled near-field tip−sample polarization $\vec{p}$ as a vertically polarized point dipole located above the dielectric surface. Generally, when in close proximity to a dielectric surface the emission pattern of a dipole is modified via near-field coupling between the dipole and propagating photons within the surface.[35] The angular distribution and total emitted power P_e of a dipole on the prism surface is given by

$$P_e(n, \theta) = \frac{3}{8\pi}\frac{n^5}{n^2 - 1}[(n^2 + 1)\sin^2(\theta) - 1]^{-1}\sin^2(2\theta)$$

where θ is the angle from surface normal and $n = n_2/n_2$ is the ratio of the refractive indices of the prism n_2 and the liquid n_1.

Figure 2b shows the angular distribution of P_e for a dipole in water ($n_1 = n_2$ = 1.265) compared to the same dipole in water when located on the ZnSe prism surface ($n_1 = n_2$ = 1.265, n_2 = 2.43) both calculated at $\bar{\nu}$ = 1660 cm^{-1}. The free space dipole emission follows the expected $\sin^2\theta$ angular dependence. However, in the presence of a dielectric surface, the emission peaks at angles close to the critical angle and can far exceed emission strength in the absence of the dielectric due to evanescent near-field coupling of high wavevector components of the dipole field to free space forbidden photon modes. In the case of ZnSe (n = 2.43), the emission peaks at θ_c = 58° and exceeds the free space value by over an order of magnitude. The resulting highly directional emission can then be efficiently collected by the solid angle of the parabolic mirror (red-shaded region).

Figure 2c shows the transmission coefficient T, the total dipole emission P_e, and the collectable dipole emission TP_e from the tip as a function of the prism index of refraction. Each quantity is integrated over the solid angle of the parabolic mirror. The collected emission (blue dashed line) is maximal at a prism index of refraction of $n_2 \approx 2$.. While higher index media can extract higher wavevector components and correspondingly higher power from the sample dipole (blue solid line), transmission out of the prism becomes weaker (red line) as the critical angle becomes closer to normal incidence. Of the common mid-IR prism materials (CaF_2 (n = 1.38), ZnSe (n = 2.43), Ge (n = 4)), ZnSe was selected due to its superior signal throughput. Note that with higher index of refraction the optical field at the sample surface is more tightly confined and thereby can result in improved near-field spatial resolution and potentially higher sensitivity.[23] The reduced transmission can be mitigated by appropriate antireflective coatings.

Spatio-Spectral Imaging. Figure 3a shows the AFM topography of an ∼10 nm thick peptoid region on the ZnSe surface imaged in water. As observed previously, the peptoid sheets have a narrow spectral response peaked around 1665 cm^{-1} primarily originating from the C═O stretching vibration (Figure 3b).[30] The narrow spectral response is a result of the absence of hydrogen bonding within the sheet which creates the secondary structures in natural proteins.[36] We acquired a series of point spectra across the edge of the peptoid sheet (white dashed line in Figure 3a). The corresponding transect of the height and the first harmonic phase signal integrated over the amide I peak is shown in Figure 3c. The phase signal

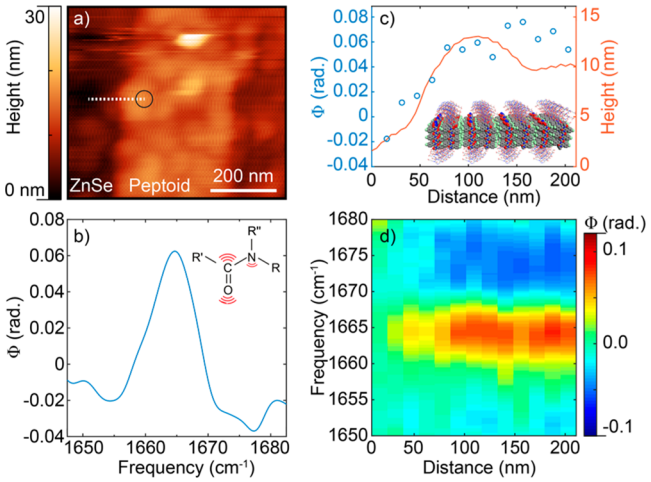

Figure 3. (a) Topography of an ∼10 nm thick section of peptoid on the ZnSe surface. (b) Point spectrum at location indicated by circle in (a). (c) Transect of optical phase integrated over 1660−1670 cm^{-1} (blue points) and topography (red) measured along the white dotted line in (a). Inset: molecular model of a monolayer of the peptoid membrane. (d) Corresponding spatio-spectral transect across peptoid edge along line indicated in (a). Spectra were obtained in 80 s with 2.5 cm^{-1} spectral resolution with a total acquisition time of ∼19 min for the spatio-spectral transect.

https://dx.doi.org/10.1021/acs.nanolett.0c01291
Nano Lett. 2020, 20, 4497−4504

initially is low on the ZnSe surface and emerges across the peptoid edge over an ∼80 nm distance (Figure 3d).

To further increase the spectroscopic sensitivity, we employ signal enhancement from plasmonic gold nanocrystals. Gold nanotriangles with thicknesses from 10 to 100 nm, and lateral dimensions in the few-μm range exhibit plasmonic resonances in the MIR range.[37] The associated field enhancement[38] significantly increases the signal levels.[39] Figure 4a shows the

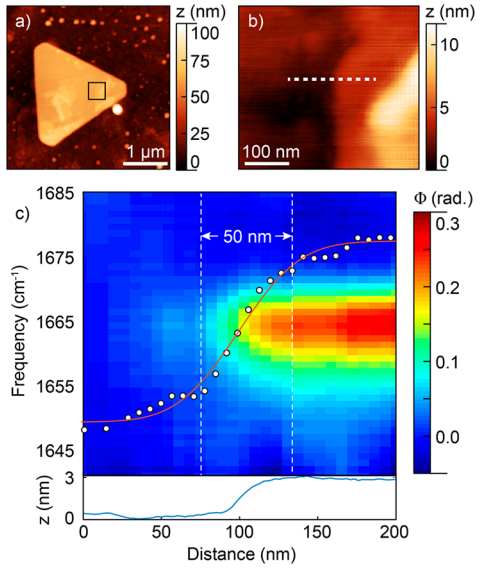

Figure 4. Spatio-spectral imaging of a monolayer peptoid nanosheet on a plasmonic gold nanostructure. (a) Topography of gold nanoprism with partial peptoid coverage. (b) Zoom-in of topography image of the area indicated by the black box in (a). (c) Spectrally resolved transect along white dashed line in (b). Each spectrum was acquired in 60 s with 4.2 cm^{-1} spectral resolution, for a total acquisition time of ∼30 min. Integrated intensity of the peptoid phase peak along transect (white circles) and corresponding error function fit (red line) indicating 80%−20% edge signal variation over ∼50 nm distance. The corresponding sample height transect is shown in the bottom panel.

topographic image of a gold nanotriangle with partial peptoid coverage. We focus on a region of monolayer peptoid nanosheet near a plasmonic node of the nanoprism (black box in Figure 4a). The topography of this region (Figure 4b) reveals an ∼4 nm thick layer, corresponding to a region of a single layer of peptoid nanosheet. We perform a spectrally resolved transect (white dashed line in Figure 4a) and probe the spatial evolution of the vibrational amide I response with high signal-to-noise (Figure 4c). The sharp amide I peak of the peptoid in the integrated phase peak intensity (from 1655 to 1675 cm^{-1}, circles) appears over ∼50 nm. The 50−80 nm width of *s*-SNOM signal variation across the peptoid edge is the result of a convolution of the tip sharpness of ∼25 nm defining nominal spatial resolution, instrument drift, and fluctuations of AFM operation in liquid, and possible inhomogeneities in the peptoid structures at their margins.

To quantify the improvement of the signal-to-noise ratio realized by plasmonic field enhancement on the gold triangle, we calculate the normalized signal-to-noise ratio (NSNR) given by $\mathrm{NSNR} = \frac{\text{signal}}{\text{noise}}/(\delta\bar{\nu}\sqrt{t})$ for both measurements where $\delta\bar{\nu}$ is the spectral resolution and t is the acquisition time. The signal level is given by the phase peak height and the noise is given by the rms deviation between repeated spectral measurements. For peptoid without the gold particle the NSNR is 0.85, whereas for the peptoid on the gold particle the NSNR is 1.1. Normalizing by the thickness of the peptoid nanosheet, this yields a factor of ∼3 improvement in sensitivity through the nanoprism plasmonic enhancement. Further improvement to the SNR could be obtained by incorporating resonant plasmonic nanostructures such as nanowires[40] or nanoslots.[41] On the basis of the ∼50−80 nm localized spectroscopic probe volume, our spectral response corresponds to 10^4 peptoid molecules or ∼20 zeptomol. Given the signal-to-noise of ∼20 of the spectrum in Figure 4, we estimate that our lower limit for detection at SNR = 3 is ∼1000 peptoids, which is comparable to results in ambient conditions.[30]

Lastly, we measure the vibrational response of a crystallized catalase nanostructure in H_2O (Figure 5a) with AFM

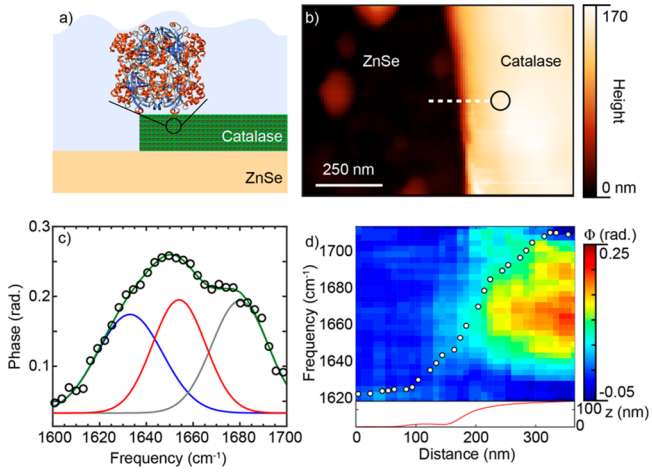

Figure 5. Spatio-spectral analysis of a catalase crystal in H_2O. (a) Sample schematic. (b) Topography of a catalase crystal. (c) Point spectrum of the catalase crystal at location indicated by black circle in (b) with fit to a sum of three Gaussian functions (red) that represent the contribution of the β-sheet (blue), α-helix (red), and β-turn (gray) conformations, respectively. (d) Spectral transect across the catalase crystal edge along white dashed line in (b). Each spectrum was acquired in 65 s at 3.8 cm^{-1} spectral resolution, for a total acquisition time of ∼28 min. White dots represent the integrated amide I peak intensity (from 1610 to 1680 cm^{-1}) as a function of distance from the catalase crystal edge and the bottom panel shows the corresponding sample height transect.

topography of the catalase crystallite shown in Figure 5b. A representative point spectrum as shown in Figure 5c (location indicated by the black circle) can be fit by a sum of three Gaussian functions centered at 1633 cm^{-1} (blue), 1654 cm^{-1} (red), and 1680 cm^{-1} (gray), corresponding to β-sheet, α-helix, and β-turn secondary structure vibrational signatures,[36] respectively, with approximately equal fractions consistent with previous results.[30,34] The spatial resolution of ∼120 nm is less than that of the peptoid sheet results above, due to the lower signal-to-noise ratio of the catalase spectrum, and the more rounded topography of the catalase crystal edge (topographic profile is shown in the lower panel of Figure 5d).

DISCUSSION

TIR *s*-SNOM leverages the vibrational sensitivity of IR spectroscopy to provide intrinsic, label-free nanoscale chemical information on biological systems in liquid. In particular, our

https://dx.doi.org/10.1021/acs.nanolett.0c01291
Nano Lett. 2020, 20, 4497−4504

results demonstrate the ability to perform chemical identification of samples in liquid with few tens of nanometers spatial resolution and bandwidth only limited by the prism transmission and the detector spectral sensitivity. Liquid EM and cryo-EM provide elemental identification of sensitive biological systems with 3D atomic resolution through its combination with computational reconstruction and either *a priori* knowledge of 1D/2D structures,[8] labeling with nanoparticles,[42] or other analytical techniques such as electron energy loss spectroscopy (EELS).[43]

The weakly perturbing nature of IR spectroscopy makes TIR *s*-SNOM well-suited for liquid phase studies of biosystems which are highly sensitive to electrical, optical, or thermal damage. Liquid cells used in electron microscopy mitigate beam damage by providing electrical and thermal conduction and have achieved nanometer spatial resolution.[1−5,42,44] However, low electron currents ($<10^2$ electrons/nm^2) are still needed to prevent damage to the comparably weak hydrogen bonds that govern the nanoscale organization of proteins and other biosystems. In contrast, TIR *s*-SNOM is intrinsically minimally invasive due to low photon energy and thermal load on the sample ($\Delta T < 1$ K).[23]

While the spatial resolution and depth sensitivity of TIR *s*-SNOM is at present limited by the apex radius of the tip to $\gtrsim$10 nm, it harnesses the intrinsic sensitivity of FTIR spectroscopy to perform chemical identification without relying on correlated compositional analyses. Complementary results can be achieved using in-liquid tip enhanced Raman spectroscopy (TERS), where chemical sensitivity of analytes in liquid with few nanometer spatial resolution has been achieved via strong plasmonically enhanced fields.[14,17,18] However, TERS measurements of biological systems in liquid have not yet been reported to date, in part due to their typically weak Raman scattering cross sections.

This work extends previous efforts of near-field imaging of biomolecules in liquid. Prior in-liquid applications of aperture-type scanning near-field optical microscopy (*a*-SNOM) have minimized absorption by using tapered metallized optical fibers as local optical probes.[45−49] However, the spatial resolution in *a*-SNOM is generally worse than in *s*-SNOM due to the reduction of collection efficiency with decreasing nanoscopic fiber aperture diameter. As a result, while ∼50 nm spatial resolution has been demonstrated at visible wavelengths,[47,49] only ∼1 μm spatial resolution has been achieved at infrared frequencies due to the longer wavelength and reduced fiber transmission.[48]

Initial development of graphene-encapsulated liquid cells have allowed nanospectroscopic studies of aqueous samples using *s*-SNOM while circumventing the numerous issues of in-liquid AFM operation.[27−29] A first iteration consisted of a small volume of water enclosed in a folded graphene sheet and allowed nanospectroscopic imaging of a tobacco mosaic virus in water.[27] However, the high hydrostatic pressure of up to 1 GPa present within this geometry may distort the sample structure from its native state[23,50] and the variable water thickness may introduce image contrast artifacts.[27] More recently, graphene-encapsulated liquid cells formed by microholes in Si_3N_4 have allowed spectroscopic investigation of protein aggregates[29] and electrochemical processes;[28] however, due to their conventional free space illumination pathway these geometries have large background signals which require demodulation at higher harmonics of the tapping frequency at the expense of overall signal levels. In parallel, scanning microwave impedance microscopy (sMIM) has been applied to similar liquid-cell structures to study dynamic processes within flow cells.[51,52] While sMIM has the advantage of lower background signal, it is at the expense of lower spatial resolution and vibrational specificity.

In the TIR geometry used herein and in in-liquid PTIR, the prism with the sample is scanned during coarse positioning and imaging. This results in an effective beam path change as the amount of dielectric material in the beam focus varies with sample movement in the plane of incidence. As a result, the effective focal length varies by ∼2 μm for 1 μm lateral sample scan in the plane of incidence. While the resulting spot size variation is only ∼0.1% for typical 1 μm scan sizes, for 5 μm sample movement the spot size changes by a few percent which necessitates realignment for larger scale sample coarse positioning. In addition, the effective path length change results in a phase shift of the tip-scattered light of $\sim 0.34\pi/\mu$m for sample movement in the plane of incidence, requiring a phase correction for spatially resolved studies. This effect complicates the use of single frequency laser sources for chemically specific imaging based on phase images. However, for spatially resolved point spectroscopy as performed in this study, this phase offset is readily subtracted. While this work was limited to 1D studies to assess the spatial resolution and sensitivity of the technique, chemical nanoimaging can be performed through an extension to 2D point spectroscopy[53] or through a recently developed rotating frame approach.[54]

Despite these issues, TIR *s*-SNOM as an all-optical extension of in-liquid PTIR has several potential advantages. In PTIR, an AFM tip detects the thermal expansion force due to material IR absorption of a pulsed laser source.[55] PTIR is compatible with in-liquid operation where nanoscale spatial resolution has been demonstrated in structures of a living cell,[22] a polymer thin film,[23] peptide fibrils,[24] and phonon polariton propagation in hexagonal BN.[25] Typically, the laser intensity is periodically modulated at a frequency matching a bending mode of the cantilever. In this case, the induced cantilever motion Δz is given by $\Delta z \propto \alpha Q I$, where α is the sample absorption coefficient, Q is the quality factor of the bending mode, and I is the laser intensity. In liquid AFM operation, Q is typically lower due to high viscous damping which reduces the induced motion of the tip and in turn the sensitivity of PTIR. Additionally, contribution from the thermal expansion of the liquid itself can create a large background in measurements of thin samples which requires careful normalization[24] or the use of deuterated water with lower IR absorption in the amide I range.[23,24]

Optical detection of the vibrational sample response circumvents the difficulties of mechanical detection in PTIR. While the low *Q*-factor and generally complex and variable structure of cantilever resonance line shape can complicate AFM operation in liquid, this does not limit the sensitivity of TIR *s*-SNOM. TIR *s*-SNOM is also insensitive to the liquid thermal expansion and thus can be applied to down to monolayer sample thicknesses. However, since the excitation and collection efficiency decays exponentially in TIR *s*-SNOM, it is limited to sample thicknesses less than a few hundred nanometers in which case PTIR becomes more suitable.

Additionally, while PTIR is only sensitive to IR absorption given by the imaginary part of the index of refraction, through interferometric detection *s*-SNOM is sensitive to the optical field magnitude and phase, which provides the full dielectric response function, including dispersion, analogous to ellips-

https://dx.doi.org/10.1021/acs.nanolett.0c01291
Nano Lett. 2020, 20, 4497−4504

ometry.[56] Albeit not as relevant for probing molecular vibrational signatures, this aspect is of increased significance for Drude conductivity or collective phonon or plasmon polaritonic responses. Furthermore, TIR *s*-SNOM has less stringent requirements in terms of suitable laser sources compared to PTIR, which typically requires tunability of the repetition rate of the source.

CONCLUSION

In summary, we present the first demonstration of *s*-SNOM in liquid using a total internal reflection geometry which simultaneously achieves high spatial resolution, intrinsic chemical sensitivity, and in-liquid operation. The evanescent field sample excitation and collection pathway minimizes water IR absorption and far-field background signals, provides high field confinement at the tip apex, and efficiently couples high k-vector sample dipole field components into detectable radiation. We demonstrate nanoscale spatial resolution with conformational structural analysis of different protein and peptoid nanostructures. With the AFM fully encased in the native liquid environment this design can readily incorporate variations of pH, solvent composition, and temperature. This new approach thus provides a broadly applicable platform for in situ infrared vibrational nanospectroscopy for the study of chemical, biological, and electrochemical processes, for example, pH-induced protein folding[20,57] or the formation of a passivation layer on battery electrodes.[58]

METHODS

The tip-scattered light collected with the off-axis parabolic mirror (OAPM) is combined with light from a reference arm in an asymmetric Michelson geometry and detected with a liquid nitrogen cooled MgCdTe detector (MN: J15D12-500-S050U-30-WE, Judson). The detector signal is amplified and sent to a lock-in detector (MN: HF2LI, Zurich) which demodulates the optical signal at harmonics of the tip-tapping frequency Ω to filter out background from far-field scattering. Interferograms are collected by sweeping the reference arm position using a closed-loop nanopositioning stage (MN: ANT95L, Aerotech). To remove the instrument response from the spectra, the phase spectrum is normalized by a reference spectrum obtained on a bare ZnSe region to obtain $\Phi = \Phi_{samp} - \Phi_{ref}$. An offset is also subtracted from the phase spectra to correct for the spatially varying phase change due to lateral movement of the sample prism. We use gold coated tips (240AC-GG, OPUS) to provide strong antenna enhancement of the molecular vibrational signatures to improve sensitivity.

A Ti:sapphire oscillator (Mira-HP, Coherent) generates NIR pulses ($\lambda \simeq 800$ nm, pulse duration ~200 fs) which pump an optical parametric oscillator (Chameleon, APE) to generate NIR signal and idler beams. Difference frequency generation (Harmonixx, APE) is used to generate ~1−2 mW of mid-infrared radiation in the amide-I spectral range with typical bandwidth of ~100 cm^{-1}.

ASSOCIATED CONTENT

Supporting Information

The Supporting Information is available free of charge at https://pubs.acs.org/doi/10.1021/acs.nanolett.0c01291.

Additional FDTD simulations illustrating the effect of a nonuniform Au film on the field strength between the tip and the sample, as well a comparison of the spatial extent of the enhanced electric field on the ZnSe surface versus on a Au surface (PDF)

AUTHOR INFORMATION

Corresponding Authors

Markus B. Raschke − *Department of Physics, Department of Chemistry, and JILA, University of Colorado at Boulder, Boulder, Colorado 80309, United States;* orcid.org/0000-0003-2822-851X; Email: markus.raschke@colorado.edu

A. Scott Lea − *Environmental Molecular Sciences Laboratory, Pacific Northwest National Laboratory, Richland, Washington 99352, United States;* orcid.org/0000-0002-4232-1553; Email: scott.lea@pnnl.gov

Authors

Brian T. O'Callahan − *Environmental Molecular Sciences Laboratory, Pacific Northwest National Laboratory, Richland, Washington 99352, United States;* orcid.org/0000-0001-9835-3207

Kyoung-Duck Park − *Department of Physics, School of Natural Science, Ulsan National Institute of Science and Technology (UNIST), Ulsan 44919, Republic of Korea;* orcid.org/0000-0002-9302-9384

Irina V. Novikova − *Environmental Molecular Sciences Laboratory, Pacific Northwest National Laboratory, Richland, Washington 99352, United States*

Tengyue Jian − *Physical Sciences Division, Pacific Northwest National Laboratory, Richland, Washington 99352, United States;* orcid.org/0000-0002-4463-5492

Chun-Long Chen − *Physical Sciences Division, Pacific Northwest National Laboratory, Richland, Washington 99352, United States;* orcid.org/0000-0002-5584-824X

Eric A. Muller − *Department of Physics, Department of Chemistry, and JILA, University of Colorado at Boulder, Boulder, Colorado 80309, United States;* orcid.org/0000-0002-9629-1767

Patrick Z. El-Khoury − *Physical Sciences Division, Pacific Northwest National Laboratory, Richland, Washington 99352, United States;* orcid.org/0000-0002-6032-9006

Complete contact information is available at: https://pubs.acs.org/10.1021/acs.nanolett.0c01291

Author Contributions

B.T.O. performed the data collection and analysis. K-D.P. performed the FDTD simulations and refinement of experimental geometry. I.V.N. provided the catalase crystallites. and T.J. and C.L.C. provided the peptoid samples. E.A.M. and M.B.R. developed the experimental concept. P.Z., E-K., and A.S.L. provided experimental guidance and advice.

Notes

The authors declare no competing financial interest.

ACKNOWLEDGMENTS

A.S.L., B.T.O., M.B.R, and P.Z.E. are supported by the Department of Energy (DOE), Office of Science, Biological and Environmental Research (BER) Bioimaging Technology project no. 69212. M.B.R. also acknowledges STROBE, a National Science Foundation Science and Technology Center (Grant DMR 1548924). The preparation of peptoid nanosheets was supported by the DOE Office of Basic Energy Sciences, and Biomolecular Materials Program at PNNL. K.-D. P. is supported by the National Research Foundation of Korea

(NRF) grant funded by the Korea government (MEST) (No. NRF-2019R1F1A1059892). This work was performed in the Environmental Molecular Sciences Laboratory (EMSL), a DOE Office of Science User Facility sponsored by BER and located at Pacific Northwest National Laboratory (PNNL). PNNL is operated by Battelle Memorial Institute for the DOE under contract number DE-AC05-76RL1830.

REFERENCES

(1) Parsons, D. F. Structure of Wet Specimens in Electron Microscopy. *Science* **1974**, *186* (4162), 407−414.
(2) Zheng, H.; Smith, R. K.; Jun, Y.-w.; Kisielowski, C.; Dahmen, U.; Alivisatos, A. P. Observation of Single Colloidal Platinum Nanocrystal Growth Trajectories. *Science* **2009**, *324* (5932), 1309−1312.
(3) de Jonge, N.; Poirier-Demers, N.; Demers, H.; Peckys, D. B.; Drouin, D. Nanometer-resolution electron microscopy through micrometers-thick water layers. *Ultramicroscopy* **2010**, *110* (9), 1114−1119.
(4) Stokes, D. J. *Principles and Practice of Variable Pressure/Environmental Scanning Electron Microscopy (VP-ESEM)*; Wiley, 2008.
(5) Stokes, D. J. Recent advances in electron imaging, image interpretation and applications: environmental scanning electron microscopy. *Philos. Trans. R. Soc., A* **2003**, *361* (1813), 2771−2787.
(6) Hui, S. W.; Parsons, D. F. Electron Diffraction of Wet Biological Membranes. *Science* **1974**, *184* (4132), 77−78.
(7) Ross, F. M. Opportunities and challenges in liquid cell electron microscopy. *Science* **2015**, *350* (6267), No. aaa9886.
(8) Puchades, C.; Rampello, A. J.; Shin, M.; Giuliano, C. J.; Wiseman, R. L.; Glynn, S. E.; Lander, G. C. Structure of the mitochondrial inner membrane AAA+ protease YME1 gives insight into substrate processing. *Science* **2017**, *358* (6363), No. eaao0464.
(9) Shtengel, G.; et al. Interferometric fluorescent super-resolution microscopy resolves 3D cellular ultrastructure. *Proc. Natl. Acad. Sci. U. S. A.* **2009**, *106* (9), 3125−3130.
(10) Klar, T. A.; Jakobs, S.; Dyba, M.; Egner, A.; Hell, S. W. Fluorescence microscopy with diffraction resolution barrier broken by stimulated emission. *Proc. Natl. Acad. Sci. U. S. A.* **2000**, *97* (15), 8206−8210.
(11) Dickson, R. M.; Cubitt, A. B.; Tsien, R. Y.; Moerner, W. E. On/off blinking and switching behaviour of single molecules of green fluorescent protein. *Nature* **1997**, *388* (6640), 355−358.
(12) Shroff, H.; Galbraith, C. G.; Galbraith, J. A.; Betzig, E. Live-cell photoactivated localization microscopy of nanoscale adhesion dynamics. *Nat. Methods* **2008**, *5* (5), 417−423.
(13) Rust, M. J.; Bates, M.; Zhuang, X. Sub-diffraction-limit imaging by stochastic optical reconstruction microscopy (STORM). *Nat. Methods* **2006**, *3* (10), 793−796.
(14) Bhattarai, A.; El-Khoury, P. Z. Nanoscale Chemical Reaction Imaging at the Solid-Liquid Interface via TERS. *J. Phys. Chem. Lett.* **2019**, *10* (11), 2817−2822.
(15) Berweger, S.; Nguyen, D. M.; Muller, E. A.; Bechtel, H. A.; Perkins, T. T.; Raschke, M. B. Nano-Chemical Infrared Imaging of Membrane Proteins in Lipid Bilayers. *J. Am. Chem. Soc.* **2013**, *135* (49), 18292−18295.
(16) Lu, F.; Jin, M.; Belkin, M. A. Tip-enhanced infrared nanospectroscopy via molecular expansion force detection. *Nat. Photonics* **2014**, *8*, 307−312.
(17) Bhattarai, A.; Joly, A. G.; Krayev, A.; El-Khoury, P. Z. Taking the Plunge: Nanoscale Chemical Imaging of Functionalized Gold Triangles in H2O via TERS. *J. Phys. Chem. C* **2019**, *123* (12), 7376−7380.
(18) Kumar, N.; Su, W.; Veselý, M.; Weckhuysen, B. M.; Pollard, A. J.; Wain, A. J. Nanoscale chemical imaging of solid-liquid interfaces using tip-enhanced Raman spectroscopy. *Nanoscale* **2018**, *10* (4), 1815−1824.
(19) Chi, Z.; Chen, X. G.; Holtz, J. S. W.; Asher, S. A. UV Resonance Raman-Selective Amide Vibrational Enhancement: Quantitative Methodology for Determining Protein Secondary Structure. *Biochemistry* **1998**, *37* (9), 2854−2864.
(20) Etezadi, D.; Warner, J. B.; Lashuel, H. A.; Altug, H. Real-Time In Situ Secondary Structure Analysis of Protein Monolayer with Mid-Infrared Plasmonic Nanoantennas. *ACS Sens.* **2018**, *3*, 1109−1117.
(21) Baker, M. J.; et al. Using Fourier transform IR spectroscopy to analyze biological materials. *Nat. Protoc.* **2014**, *9*, 1771−1791.
(22) Mayet, C.; Dazzi, A.; Prazeres, R.; Allot, F.; Glotin, F.; Ortega, J. M. Sub-100 nm IR spectromicroscopy of living cells. *Opt. Lett.* **2008**, *33* (14), 1611−1613.
(23) Jin, M.; Lu, F.; Belkin, M. A. High-sensitivity infrared vibrational nanospectroscopy in water. *Light: Sci. Appl.* **2017**, *6*, No. e17096.
(24) Ramer, G.; Ruggeri, F. S.; Levin, A.; Knowles, T. P. J.; Centrone, A. Determination of Polypeptide Conformation with Nanoscale Resolution in Water. *ACS Nano* **2018**, *12* (7), 6612−6619.
(25) Wang, H.; Janzen, E.; Wang, L.; Edgar, J. H.; Xu, X. G., Probing Mid-Infrared Phonon Polaritons in the Aqueous Phase. *Nano Lett.* **2020**, DOI: 10.1021/acs.nanolett.0c01199.
(26) Amenabar, I.; et al. Structural analysis and mapping of individual protein complexes by infrared nanospectroscopy. *Nat. Commun.* **2013**, *4*, 2890.
(27) Khatib, O.; et al. Graphene-Based Platform for Infrared Near-Field Nanospectroscopy of Water and Biological Materials in an Aqueous Environment. *ACS Nano* **2015**, *9* (8), 7968−7975.
(28) Lu, Y.-H.; Larson, J. M.; Baskin, A.; Zhao, X.; Ashby, P. D.; Prendergast, D.; Bechtel, H. A.; Kostecki, R.; Salmeron, M. Infrared Nanospectroscopy at the Graphene-Electrolyte Interface. *Nano Lett.* **2019**, *19* (8), 5388−5393.
(29) Meireles, L. M.; Barcelos, I. D.; Ferrari, G. A.; de A. Neves, P. A. A.; Freitas, R. O.; Lacerda, R. G. Synchrotron infrared nanospectroscopy on a graphene chip. *Lab Chip* **2019**, *19*, 3678−3684.
(30) O'Callahan, B. T.; Crampton, K. T.; Novikova, I. V.; Jian, T.; Chen, C.-L.; Evans, J. E.; Raschke, M. B.; El-Khoury, P. Z.; Lea, A. S. Imaging Nanoscale Heterogeneity in Ultrathin Biomimetic and Biological Crystals. *J. Phys. Chem. C* **2018**, *122* (43), 24891−24895.
(31) Raschke, M. B.; Lienau, C. Apertureless near-field optical microscopy: Tip-sample coupling in elastic light scattering. *Appl. Phys. Lett.* **2003**, *83* (24), 5089−5091.
(32) Jin, H.; Jiao, F.; Daily, M. D.; Chen, Y.; Yan, F.; Ding, Y.-H.; Zhang, X.; Robertson, E. J.; Baer, M. D.; Chen, C.-L. Highly stable and self-repairing membrane-mimetic 2D nanomaterials assembled from lipid-like peptoids. *Nat. Commun.* **2016**, *7*, 12252.
(33) Nannenga, B. L.; Shi, D.; Hattne, J.; Reyes, F. E.; Gonen, T. Structure of catalase determined by MicroED. *eLife* **2014**, *3*, No. e03600.
(34) Vainshtein, B. K.; Melik-Adamyan, W. R.; Barynin, V. V.; Vagin, A. A.; Grebenko, A. I.; Borisov, V. V.; Bartels, K. S.; Fita, I.; Rossmann, M. G. Three-dimensional structure of catalase from Penicillium vitale at 2.0 Å resolution. *J. Mol. Biol.* **1986**, *188* (1), 49−61.
(35) Lukosz, W.; Kunz, R. E. Light emission by magnetic and electric dipoles close to a plane dielectric interface. II. Radiation patterns of perpendicular oriented dipoles. *J. Opt. Soc. Am.* **1977**, *67* (12), 1615−1619.
(36) Barth, A. Infrared spectroscopy of proteins. *Biochim. Biophys. Acta, Bioenerg.* **2007**, *1767* (9), 1073−1101.
(37) Jones, A. C.; Olmon, R. L.; Skrabalak, S. E.; Wiley, B. J.; Xia, Y. N.; Raschke, M. B. Mid-IR Plasmonics: Near-Field Imaging of Coherent Plasmon Modes of Silver Nanowires. *Nano Lett.* **2009**, *9* (7), 2553−2558.
(38) Dregely, D.; Neubrech, F.; Duan, H.; Vogelgesang, R.; Giessen, H. Vibrational near-field mapping of planar and buried three-dimensional plasmonic nanostructures. *Nat. Commun.* **2013**, *4* (1), 2237.
(39) Neubrech, F.; Huck, C.; Weber, K.; Pucci, A.; Giessen, H. Surface-Enhanced Infrared Spectroscopy Using Resonant Nano-antennas. *Chem. Rev.* **2017**, *117* (7), 5110−5145.

https://dx.doi.org/10.1021/acs.nanolett.0c01291
Nano Lett. 2020, 20, 4497−4504

(40) O'Callahan, B. T.; Hentschel, M.; Raschke, M. B.; El-Khoury, P. Z.; Lea, A. S. Ultrasensitive Tip- and Antenna-Enhanced Infrared Nanoscopy of Protein Complexes. *J. Phys. Chem. C* **2019**, *123* (28), 17505−17509.
(41) Yang, H. U.; Olmon, R. L.; Deryckx, K. S.; Xu, X. G.; Bechtel, H. A.; Xu, Y.; Lail, B. A.; Raschke, M. B. Accessing the Optical Magnetic Near-Field through Babinet's Principle. *ACS Photonics* **2014**, *1* (9), 894−899.
(42) Jonge, N. d.; Peckys, D. B.; Kremers, G. J.; Piston, D. W. Electron microscopy of whole cells in liquid with nanometer resolution. *Proc. Natl. Acad. Sci. U. S. A.* **2009**, *106* (7), 2159−2164.
(43) Wang, C.; Qiao, Q.; Shokuhfar, T.; Klie, R. F. High-Resolution Electron Microscopy and Spectroscopy of Ferritin in Biocompatible Graphene Liquid Cells and Graphene Sandwiches. *Adv. Mater.* **2014**, *26* (21), 3410−3414.
(44) de Jonge, N.; Ross, F. M. Electron microscopy of specimens in liquid. *Nat. Nanotechnol.* **2011**, *6*, 695−704.
(45) Subramaniam, V.; Kirsch, A. K.; Rivera-Pomar, R. V.; Jovin, T. M. Scanning Near-Field Optical Microscopy and Microspectroscopy of Green Fluorescent Protein in Intact Escherichia coli Bacteria. *J. Fluoresc.* **1997**, *7* (4), 381−385.
(46) Muramatsu, H.; Homma, K.; Yamamoto, N.; Wang, J.; Sakata-Sogawa, K.; Shimamoto, N. Imaging of DNA molecules by scanning near-field microscope. *Mater. Sci. Eng., C* **2000**, *12* (1), 29−32.
(47) Muramatsu, H.; Chiba, N.; Ataka, T.; Iwabuchi, S.; Nagatani, N.; Tamiya, E.; Fujihira, M. Scanning Near-Field Optical/Atomic Force Microscopy for Fluorescence Imaging and Spectroscopy of Biomaterials in Air and Liquid: Observation of Recombinant Escherichia coli with Gene Coding to Green Fluorescent Protein*. *Opt. Rev.* **1996**, *3* (6B), 470−474.
(48) Platkov, M.; Tsun, A.; Nagli, L.; Katzir, A. A scanning near-field middle-infrared microscope for the study of objects submerged in water. *Appl. Phys. Lett.* **2008**, *92* (10), 104104.
(49) Park, K.-D.; Raschke, M. B.; Jang, M. J.; Kim, J. H.; O, B.-H.; Park, S.-G.; Lee, E.-H.; Lee, S. G. Near-Field Imaging of Cell Membranes in Liquid Enabled by Active Scanning Probe Mechanical Resonance Control. *J. Phys. Chem. C* **2016**, *120* (37), 21138−21144.
(50) Algara-Siller, G.; Lehtinen, O.; Wang, F. C.; Nair, R. R.; Kaiser, U.; Wu, H. A.; Geim, A. K.; Grigorieva, I. V. Square ice in graphene nanocapillaries. *Nature* **2015**, *519*, 443−445.
(51) Tselev, A.; Fagan, J.; Kolmakov, A. In-situ near-field probe microscopy of plasma processing. *Appl. Phys. Lett.* **2018**, *113* (26), 263101.
(52) Tselev, A.; Velmurugan, J.; Ievlev, A. V.; Kalinin, S. V.; Kolmakov, A. Seeing through Walls at the Nanoscale: Microwave Microscopy of Enclosed Objects and Processes in Liquids. *ACS Nano* **2016**, *10* (3), 3562−3570.
(53) Muller, E. A.; Gray, T. P.; Zhou, Z.; Cheng, X.; Khatib, O.; Bechtel, H. A.; Raschke, M. B. Vibrational exciton nanoimaging of phases and domains in porphyrin nanocrystals. *Proc. Natl. Acad. Sci. U. S. A.* **2020**, *117* (13), 7030−7037.
(54) Johnson, S. C.; Muller, E. A.; Khatib, O.; Bonnin, E. A.; Gagnon, A. C.; Raschke, M. B. Infrared nanospectroscopic imaging in the rotating frame. *Optica* **2019**, *6* (4), 424−429.
(55) Dazzi, A.; Prater, C. B. AFM-IR: Technology and Applications in Nanoscale Infrared Spectroscopy and Chemical Imaging. *Chem. Rev.* **2017**, *117* (7), 5146−5173.
(56) Olmon, R. L.; Rang, M.; Krenz, P. M.; Lail, B. A.; Saraf, L. V.; Boreman, G. D.; Raschke, M. B. Determination of Electric-Field, Magnetic-Field, and Electric-Current Distributions of Infrared Optical Antennas: A Near-Field Optical Vector Network Analyzer. *Phys. Rev. Lett.* **2010**, *105* (16), 167403.
(57) Semenyshyn, R.; Hentschel, M.; Stanglmair, C.; Teutsch, T.; Tarin, C.; Pacholski, C.; Giessen, H.; Neubrech, F. In Vitro Monitoring Conformational Changes of Polypeptide Monolayers Using Infrared Plasmonic Nanoantennas. *Nano Lett.* **2019**, *19*, 1−7.
(58) Shi, F.; Ross, P. N.; Somorjai, G. A.; Komvopoulos, K. The Chemistry of Electrolyte Reduction on Silicon Electrodes Revealed by in Situ ATR-FTIR Spectroscopy. *J. Phys. Chem. C* **2017**, *121* (27), 14476−14483.

https://dx.doi.org/10.1021/acs.nanolett.0c01291
Nano Lett. 2020, 20, 4497−4504